A new parameterization of coastal drag to simulate landfast ice in deep marginal seas in the Arctic

Yuqing Liu[1], Martin Losch[1], Nils Hutter[1,2], Longjiang Mu[3]

[1]Alfred-Wegener-Institut, Helmholtz-Zentrum für Polar-und Meeresforschung, Bremerhaven, Germany
[2]Cooperative Institute for Climate, Ocean and Ecosystem Studies, University of Washington, Seattle, WA, USA
[3]Pilot National Laboratory for Marine Science and Technology, Qingdao, China

Key Points:

- A new lateral drag parameterization improves landfast ice simulations in the Kara Sea
- A static friction law describes the lateral drag between sea ice and the coast
- The combination of lateral drag and grounding parameterization leads to the best agreement with observations

Corresponding author: Yuqing Liu, yuqing.liu@awi.de

Abstract

Landfast ice is nearly immobile sea ice attached to the coast. Despite the important role of landfast ice in coastal climates, landfast ice is not well simulated in current sea ice models and needs to be parameterized. The mechanism for landfast ice formation is linked to the local geography. Grounded ice ridges act as anchoring points in shallow water. Sea ice arching between offshore island chains can lead to landfast ice in deep water. Previous studies successfully represented landfast ice in shallow marginal seas using bathymetry information to implement a grounding scheme, but this method fails in deep regions. This paper develops a new parameterization for coarse resolution sea ice models using lateral drag as a function of sea ice thickness, drift velocity, and coastline length. The new parameterization is tested in a 36 km pan-Arctic sea ice-ocean simulation. The simulated landfast ice in the model run is compared to observations from satellite data. With the lateral drag parameterization, representation of landfast ice improves in deep marginal seas. The combination of the lateral drag parameterization and a grounding scheme leads to a realistic landfast ice distribution in most Arctic regions.

Plain Language Summary

Landfast ice is nearly immobile sea ice attached to the coast. In the Arctic, landfast ice is found along the coasts of the marginal shelf seas as a seasonally stable ice cover that inhibits heat exchange between the atmosphere and the ocean. It also serves local communities as a means of traveling. Two main processes have been identified that lead to landfast ice: grounding in shallow water, and static arching between pinning points such as islands. In numerical computer models of the Arctic, these mechanisms are typically not resolved and need to be parameterized for the models to simulate realistic landfast ice distributions. As an enhancement to an established parameterization scheme for grounding, we present a new parameterization for the pinning effect of unresolved coastline features and islands. With this new parameterization, the model results improve compared to satellite-based observational data, especially in the deep shelf regions of the Kara Sea with water depths below 30m. The best overall agreement between model results and observations in most Arctic regions is found when the new parameterization and the grounding scheme are combined.

1 Introduction

Landfast ice is defined as "sea ice that stays fast along the coast where it is attached to the shore, to an ice wall, to an ice front, or over shoals, or between grounded icebergs." (World Meteorological Organization, 2014). Landfast ice is a common phenomenon in polar winter. It forms in the fall as onshore winds thicken and consolidate the ice along the shore until it breaks up in spring. The extent of landfast ice in the Arctic varies with water depth and slope of the continental shelf (Yu et al., 2014; Kwok, 2018). Anchored pressure ridges ground coastal sea ice all along the coast of Alaska and the Laptev Sea. Landfast ice can also be formed in deep marginal regions by lateral propagation of internal stresses from contact points with the coastline, as seen in the Kara Sea (Li et al., 2020). Furthermore, landfast ice can also be landlocked ice that is confined in the narrow channels of the Canadian Arctic Archipelago (Melling, 2002; Howell et al., 2016).

Landfast ice is likely a sensitive indicator of climate change (A. Mahoney et al., 2007). Since it is immobile, landfast ice prevents sea ice compression in convergence, limiting sea ice thickness (Itkin et al., 2015). Landfast ice also decreases the transfer of heat, moisture, and momentum between the atmosphere and the ocean in coastal areas (Lemieux et al., 2016). The extent of landfast ice regulates the location of flaw polynyas or flaw leads (the openings between the landfast ice and pack ice, Itkin et al., 2015). Landfast ice also has an effect on simulating sea surface height (Proshutinsky et al., 2007) and sea ice thickness (Johnson et al., 2012).

Landfast ice is an important feature in coastal regions, but most large-scale sea ice models underestimate the extent of landfast ice (Lemieux et al., 2018). Several attempts have been made to improve the simulation of landfast ice in these models. Beatty and Holland (2010) added isotropic tensile strength to a viscous-plastic sea ice model (Hibler, 1979) to simulate landfast ice. Itkin et al. (2015) simulated landfast ice by adding tensile strength to the sea ice rheology in regions shallower than 25 m and found that landfast ice affected the stability of the halocline in the Arctic. Olason (2016) was able to simulate landfast ice in the Kara Sea by increasing the maximum sea ice viscosity, a parameter that regularizes the momentum equation of sea ice, but left the appropriate value of maximum viscosity an open question. Olason (2016) also reported that the landfast ice in the Kara Sea was primarily supported by static arching, which was consistent with observations suggesting that a chain of offshore islands provides anchoring points for the

landfast ice in the Kara Sea (Divine et al., 2005). Lemieux et al. (2015) parameterized grounding of ice keels by a basal stress term as a function of topography and sea ice thickness to enhance the representation of landfast ice in shallow regions, but the landfast ice in deep water (i.e., in the Kara Sea) was still systematically underestimated. Lemieux et al. (2016) used a combination of basal stress parameterization and tensile strength to enhance the simulation of landfast ice in deep water, but the simulated landfast ice seasons for the Kara Sea were too short compared to the satellite data.

In this study, we directly parameterize the effects of partly unresolved coastlines and islands as obstacles to sea ice motion by a lateral drag term in the sea ice momentum equation with the aim of improving landfast ice representation in the Arctic. Different approaches are tested to explore the best representation of the lateral drag stress. As previous studies (Lemieux et al., 2015, 2016; Olason, 2016), we focus on the Arctic marginal seas, in particular the Kara Sea. The landlocked landfast ice in the Canadian Arctic Archipelago is governed by different dynamics and requires different parameterisations (Lemieux et al., 2018).

The paper is organized as follows: the model configuration and experiment setup are described in Section 2, the lateral drag parameterization is shown in Section 3, the model results are presented in Section 4, the discussion and summary are given in Section 5 and Section 6.

2 Methods and data

2.1 Satellite observations

We used landfast ice records of satellite data from the National Ice Center (NIC) Arctic Sea Ice Charts and Climatologies (National Ice Center, Compiled by F. Fetterer and C. Fowler, 2009). The data is available weekly (January 1972 through June 2001) and biweekly (July 2001 through December 2007) on a 25 km Equal-Area Scalable Earth Grid. The sea ice concentration (SIC) ranges from 0% to 100% with landfast ice flagged. NIC charts are produced by manual analysis of in situ, air reconnaissance, remote sensing, and model data. We choose the biweekly files (2001 through 2007) for direct comparison to previous results using a grounding scheme (Lemieux et al., 2015, 2016).

2.2 Model simulations

All simulations in this paper are based on a regional Arctic configuration of the Massachusetts Institute of Technology general circulation model (MITgcm, Marshall et al., 1997; MITgcm Group, 2020) with a grid resolution of 36 km, similar to the configuration of Ungermann and Losch (2018). This configuration applies zero-layer thermodynamics and viscous-plastic dynamics with the solver introduced by Zhang and Hibler (1997). The model is forced by six-hourly atmospheric fields from the European Centre for Medium-Range Weather Forecasts (ECMWF) ERA-Interim data (Berrisford et al., 2011). The hydrography is initialized with temperature and salinity fields from the Polar Science Center Hydrographic Climatology 3.0 (PHC-3.0, Steele et al., 2001). Details of the sea ice model can be found in Losch et al. (2010) or the online documentation (`https://mitgcm.org`).

The model solves the two-dimensional sea ice momentum equation:

$$m\frac{\partial \mathbf{u}}{\partial t} = -mf\mathbf{k}\times\mathbf{u} + \boldsymbol{\tau}_a + \boldsymbol{\tau}_o + \boldsymbol{\tau}_b + \boldsymbol{\tau}_l - mg\nabla H + \nabla\cdot\boldsymbol{\sigma}, \tag{1}$$

where $m = \rho_i h$ is sea ice mass per grid cell area, f is the Coriolis parameter, $\mathbf{k}$ is the vertical unit vector, $\boldsymbol{\tau}_a$ and $\boldsymbol{\tau}_o$ are ice-atmosphere and ice-ocean interfacial stresses, g is the gravitational acceleration, ∇H is the gradient of the sea surface height, and $\boldsymbol{\sigma}$ is the (vertically integrated) stress tensor. Nonlinear momentum advection is neglected. The horizontal ice velocity $\mathbf{u} = u\mathbf{i} + v\mathbf{j}$ advects the mean sea ice thickness h and sea ice concentration A (Losch et al., 2010). Following Lemieux et al. (2015), the basal stress term $\boldsymbol{\tau}_b$ is zero when the ice thickness h is smaller than a critical mean thickness $h_c = A\,h_w/k_1$ where h_w is the water depth. For thicknesses larger than h_c, the basal stress is given by $\boldsymbol{\tau}_b = k_2 \frac{\boldsymbol{u}}{|\boldsymbol{u}|+u_0}(h-h_c)\,e^{-C_b(1-A)}$. Here, $C_b = 20$, $|\mathbf{u}| = \sqrt{u^2+v^2}$, and u_0 is a small velocity parameter to avoid divisions by zero. k_1 and k_2 are the tuning parameters of the grounding scheme. $\boldsymbol{\tau}_l$ is a new lateral drag stress term described in the next section.

Two parameters distinguish landfast ice from drift ice: it is attached to the coast, and it moves very little (Zhai et al., 2021; A. Mahoney et al., 2007; A. R. Mahoney et al., 2014). We classify sea ice as landfast ice when the biweekly average sea ice drift velocity is below a critical value of $5\times10^{-4}\,\mathrm{m\,s^{-1}}$ (Lemieux et al., 2015). This corresponds to a displacement of approximately 600 meters in two weeks. In addition, landfast ice is assumed to be compact with a SIC larger than 95%.

3 Lateral drag parameterization

3.1 Boundary condition

The lateral boundary conditions have a profound influence on the lateral friction and the vorticity at the boundaries (Adcroft & Marshall, 1998). Generally, the lateral boundary conditions for velocity are either no-slip or free-slip, or a mix of both. The no-slip boundary condition assumes that the fluid in direct contact with the boundary has the same velocity as this boundary (Rapp, 2017). Therefore, the tangent flow is zero on the boundary. For a C-grid with staggered velocities, this can be implemented using "ghost points" outside the domain. For example, for the tangential component u of the velocity along a boundary b in the x-direction between grid indices j and $j+1$ we have:

$$u\Big|_b \approx \frac{u_j + u_{j+1}}{2} = 0 \Leftrightarrow u_{j+1} = -u_j. \tag{2}$$

A slip boundary condition assumes a discontinuity in the velocity function (i.e., a relative movement between the fluid and the boundary). For the free-slip boundary condition the tangent shear vanishes on the boundary and the tangent flows remain finite (Rapp, 2017):

$$\frac{\partial u}{\partial y}\Big|_b \approx \frac{u_{j+1} - u_j}{\Delta y} = 0 \Leftrightarrow u_{j+1} = u_j. \tag{3}$$

In the following, we use a simple finite difference discretization model to illustrate the lateral friction on the boundary. Note that MITgcm implements a finite volume discretization, which would complicate the discussion unnecessarily. We assume a constant viscosity coefficient ν and constant grid spacing Δy for the lateral friction term in the y-direction. The lateral friction term (viscosity) along the boundary is a function of the tangential velocity u:

$$\begin{aligned} \partial_y \nu \partial_y u &= \partial_y (\nu \partial_y u) \\ &= \frac{(\nu \partial_y u)|_{j+\frac{1}{2}} - (\nu \partial_y u)|_{j-\frac{1}{2}}}{\Delta y} \\ &= \frac{1}{\Delta y}\left(\nu \frac{u_{j+1} - u_j}{\Delta y} - \nu \frac{u_j - u_{j-1}}{\Delta y}\right). \end{aligned} \tag{4}$$

For the no-slip boundary condition Equation (2), the lateral friction term becomes:

$$\partial_y \nu \partial_y u = -\frac{\nu(u_j - u_{j-1})}{(\Delta y)^2} - \frac{2\nu\, u_j}{(\Delta y)^2}. \tag{5}$$

For the free-slip boundary condition Equation (3), the lateral friction term is:

$$\partial_y \nu \partial_y u = \frac{-\nu(u_j - u_{j-1})}{(\Delta y)^2}. \tag{6}$$

Typically, sea ice models use a no-slip boundary condition to parameterize any unresolved frictional boundary layers. Comparing Equation (5) to Equation (6), the difference between the no-slip and free-slip boundary conditions is $-\frac{2\nu\, u_j}{(\Delta y)^2}$. The key idea of our new parameterization is to replace this term, which in viscous plastic models is a complicated, nonlinear function of ice pressure and ice drift velocities, with an explicit lateral drag stress. Plausibly, the lateral drag stress term is a function of the sea ice thickness (or mass), the drift velocity and the shape (i.e., resistance) of the coastline, expressed as a form factor. In its most general form, it can be written as:

$$\boldsymbol{\tau}_l = m\, F\, \mathbf{K}(\mathbf{u}), \tag{7}$$

where F is the form factor and $\mathbf{K}(\mathbf{u})$ is a function of the sea ice drift velocity $\mathbf{u}$. The form factor F depends locally on the length of the coastline and is described in details in Section 3.2. Different types of $\mathbf{K}(\mathbf{u})$ are discussed in Section 3.3.

3.2 Form factor

The form factor F is determined by the relative location of the ocean and the land within a grid cell. The model topography is interpolated from the International Bathymetric Chart of the Arctic Ocean (IBCAO) topography data (Jakobsson et al., 2012) to a 4.5 km grid and then coarse-grained to a 36 km grid. The grid is regarded as an ocean/land point if ocean/land covers more than half of the model grid (Figure 1a). Here, we discuss two types of form factors in the lateral drag parameterization. The first one F_1 is determined by the coastline resolved by the model grid, and the second F_2 uses a higher subgrid resolution coastline. As the lateral drag affects only velocities parallel to the coastline, the form factor is considered separately in the x- and y-directions. The lateral drag stress of one grid cell in the x-direction is affected by the coastline in the y-direction.

F_1^u is zero when the two neighboring model grid cells in the y-direction are both ocean points. F_1^u is one when one of the neighboring cells in the y-direction is a land point. F_1^u is two when both of the neighboring grid cells are land points. F_1^v is determined analogously. The definition for this simple form factor is summarized in Equation (8):

$$F_1^{v/u} = \begin{cases} 0, & \text{in x/y direction no land point} \\ 1, & \text{in x/y direction only one land point} \\ 2. & \text{in x/y direction two land points} \end{cases} \tag{8}$$

The second form factor F_2 involves additional sub-grid scale information provided by a high-resolution coastline data set. We use the 10 m coastline data from Natural Earth 10 m Physical Vectors (`https://www.naturalearthdata.com`). We project the 10 m coastline on the x- and y-direction within each grid cell, integrate projected natural coastline length, and normalize it by the model grid length. The normalized integrals of the 10 m coastline within one grid cell $f_2^u(i,j)$ and $f_2^v(i,j)$ are defined as:

$$f_2^u(i,j) = \frac{\sum_{n=1}^{N} |l_n \cos\theta_n|}{\Delta x_{i,j}} \tag{9}$$

$$f_2^v(i,j) = \frac{\sum_{n=1}^{N} |l_n \sin\theta_n|}{\Delta y_{i,j}}. \tag{10}$$

where $f_2^u(i,j)$ and $f_2^v(i,j)$ are projections of the 10 m coastline in the x- and y-direction normalized by the grid length. l_n is the length of the nth segment of 10 m coastline within one grid cell, θ_n is the angle between the nth 10 m coastline segment and x-axis of the model grid, $\Delta x_{i,j}$, $\Delta y_{i,j}$ are the model grid spacings in the x- and y-direction, and N is the number of 10 m coastline points within one model grid cell.

The form factors $F_2^u(i,j)$, $F_2^v(i,j)$ for $u_{i,j}$, $v_{i,j}$ are determined by f_2^u, f_2^v (Figure 1a):

$$F_2^u(i,j) = \frac{f_2^u(i,j) + f_2^u(i,j+1)}{2} \tag{11}$$

$$F_2^v(i,j) = \frac{f_2^v(i,j) + f_2^v(i+1,j)}{2}. \tag{12}$$

Figures 1b and c illustrate the two different form factors for the x-direction in the Kara Sea. Based on the high resolution coastline data, form factor F_2 is generally larger than F_1. Geographic features that are unresolved by our 36 km model grid, such as the Franz-Josef-Land archipelago, also lead to non-zero contributions to F_2, so that these features can exert lateral drag.

3.3 Function K(u)

$\mathbf{K}(\mathbf{u})$ is a function of sea ice velocity. Here we test two different forms: the first form is a quadratic function $\mathbf{K}_1(\mathbf{u}) = C_q|\mathbf{u}|\,\mathbf{u}$ similar to the ocean stress $\boldsymbol{\tau}_o$ and atmosphere stress $\boldsymbol{\tau}_a$. The second form $\mathbf{K}_2(\mathbf{u}) = C_s \frac{1}{|\mathbf{u}|+u_0}\,\mathbf{u}$ is a static friction form similar to the basal stress of Lemieux et al. (2015) with a small residual velocity u_0. C_q is the lateral drag coefficient in the quadratic function $\mathbf{K}_1(\mathbf{u})$, and C_s is the lateral drag coefficient in the static function $\mathbf{K}_2(\mathbf{u})$. The quadratic function $\mathbf{K}_1(\mathbf{u})$ increases with increasing ice movement (Figure 2). The static function $\mathbf{K}_2(\mathbf{u})$ provides constant lateral drag when sea ice drift velocity reaches the critical value $u_0 = 0.01\,\mathrm{m\,s^{-1}}$ (Figure 2).

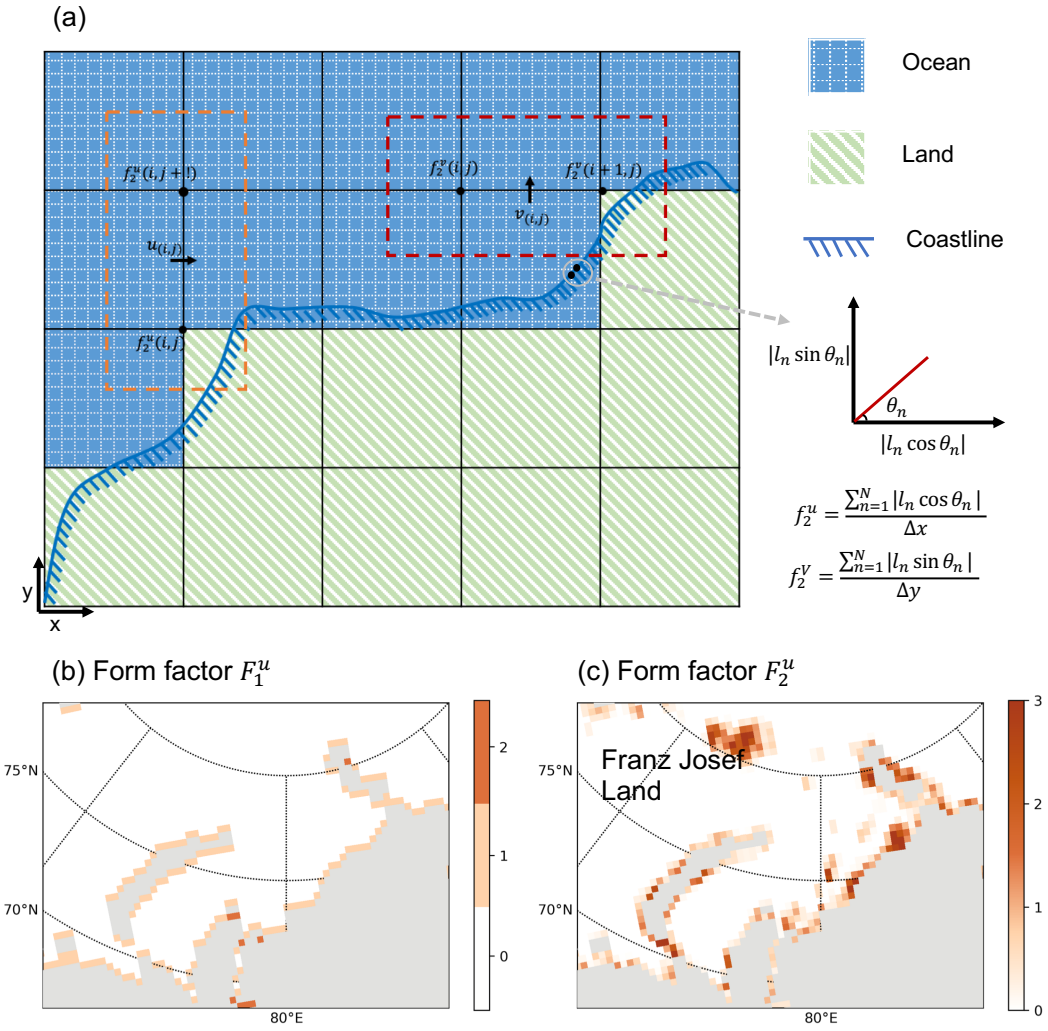

Figure 1. Definition for form factors and two form factors in x-direction in the Kara Sea. (a) Schematic illustration of form factors. The blue line represents the subgrid scale coastline. The grid pattern represents the ocean in the model, and the hashed green area is the land in the 36 km model. $f_2^u(i,j)$ and $f_2^v(i,j)$ are the projections of the subgrid scale coastline in the x- and y-direction normalized by the grid length at the grid (i,j). The point $u_{i,j}$ in the orange box is influenced by the two adjacent points and $F_2^u(i,j)$ is calculated via Equation 11. The point $v_{i,j}$ in the red box is influenced by the two surrounding points and $F_2^v(i,j)$ is defined in Equation 12. (b) and (c): The two form factors in the x-direction in the Kara Sea. Form factor F_1^u assumes values of $0, 1$, and 2. The values of F_2^u are continous.

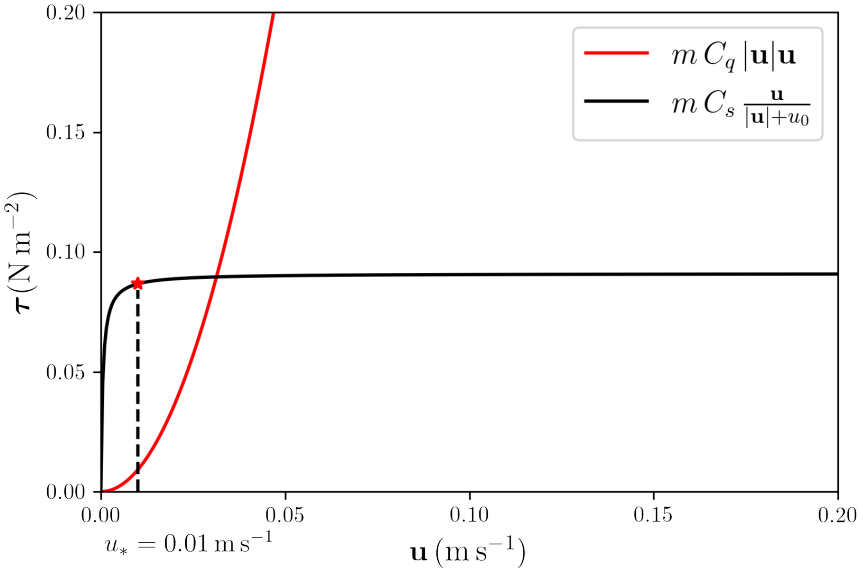

Figure 2. Quadratic and static $\mathbf{K}(\mathbf{u})$ function in the lateral drag parameterization. The red line is the quadratic function $\mathbf{K_1}(\mathbf{u})$ with $C_q = 0.1\,\mathrm{m^{-1}}$, and the black line indicates the static function of lateral drag with $C_s = 10^{-4}\,\mathrm{m\,s^{-2}}$. $m = \rho_i\,h$ is chosen as $910\,\mathrm{kg\,m^{-2}}$ corresponding to 1 m of ice. The red star denotes the threshold velocity $u_* = 0.01\,\mathrm{m\,s^{-1}}$. For the static function, the lateral drag increases quickly with sea ice drift below the threshold of $u_* = 0.01\,\mathrm{m\,s^{-1}}$ and remains almost constant above. In contrast, $\mathbf{K_1}(\mathbf{u})$ increases quadratically with velocity.

The lateral drag parameterization is mainly governed by the function $\mathbf{K}(\mathbf{u})$. To estimate the order of magnitude of lateral drag coefficients, we assume that the lateral drag term has the same order of magnitude as the wind stress term. The order of magnitude of typical wind stress in the Arctic is $0.1\,\mathrm{N\,m^{-2}}$ (Lemieux et al., 2015; Timmermans & Marshall, 2020). To reach a similar magnitude with the wind stress for the lateral drag term, we use a lateral drag coefficient $C_q = 0.1\,\mathrm{m^{-1}}$ in the quadratic function $\mathbf{K}_1(\mathbf{u})$, and $C_s = 10^{-4}\,\mathrm{m\,s^{-2}}$ for the static function $\mathbf{K}_2(\mathbf{u})$. With this choice of coefficients the different formulations give similar drag for ice velocities of $0.03\ \mathrm{m\,s^{-1}}$ (Figure 2).

Combining different form factors F and velocity function $\mathbf{K}(\mathbf{u})$, we get four formulations of the lateral drag stress terms:

$$\begin{aligned}
\boldsymbol{\tau}_{l1} &= m\,F_1\,C_q\,|\mathbf{u}|\mathbf{u} \\
\boldsymbol{\tau}_{l2} &= m\,F_2\,C_q\,|\mathbf{u}|\mathbf{u} \\
\boldsymbol{\tau}_{l3} &= m\,F_1\,C_s\,\frac{\mathbf{u}}{|\mathbf{u}| + u_0} \\
\boldsymbol{\tau}_{l4} &= m\,F_2\,C_s\,\frac{\mathbf{u}}{|\mathbf{u}| + u_0}.
\end{aligned} \tag{13}$$

4 Results

In this section, we compare experiments with different parameterizations to the satellite data of the National Ice Center (NIC) Arctic Sea Ice Charts and Climatologies (National Ice Center, Compiled by F. Fetterer and C. Fowler, 2009). To better distinguish the different model simulations, we use the abbreviations for different model simulations provided in Table 1. We first compare four lateral drag formulas, and estimate the sensitivity of the lateral drag coefficient. Next we compare the lateral and basal drag parameterization. Finally, we evaluate the time series of landfast ice extent in four marginal Arctic seas with satellite observations and assess the large-scale features in the model simulations with the new parameterization. The four marginal seas are: the Kara Sea, the Laptev Sea, the East Siberian Sea, and the Beaufort Sea. We explicitly exclude landfast ice estimates in the Canadian Arctic Archipelago, as here the dynamics are different and the model generally overestimates the landfast ice cover (Lemieux et al., 2018).

Table 1. The abbreviations of model simulations in this paper.

Abbreviation	Model simulations
CTRL	Model control run, standard 36 km model
LD	36 km model with lateral drag parameterization
BD	36 km model with basal drag parameterization
LD + BD	36 km model with both lateral and basal drag parameterization

4.1 Landfast ice frequency with different lateral drag formulas

The main aim is to improve the landfast ice representation in particular in the Kara Sea because there the water is deeper than in the other marginal seas so that landfast ice cannot form due to grounding ice keels. The landfast ice frequency in the Kara Sea from January to May in 2001–2007 was used to compare the four different lateral drag implementations shown in Equation (13). The landfast ice frequency measures the number of biweekly records with landfast ice in January to May. A value of 1 indicates that there is landfast ice in all biweekly records. Using the same form factor, the model run with the static function $\mathbf{K}_2(\mathbf{u})$ simulates larger landfast ice frequency in the Kara Sea than that with the quadratic function $\mathbf{K}_1(\mathbf{u})$ (compare Figure 3a with 3c and Figure 3b with 3d), which is more consistent with the observations (Figure 9d). With the same $\mathbf{K}(\mathbf{u})$ function, model simulations with form factor F_2 increases the landfast ice frequency in the Kara Sea compared to simulations with form factor F_1 (compare Figure 3a with 3b and Figure 3c with 3d). This supports the notion that landfast ice in the Kara Sea is mainly supported by sea ice arching as the offshore islands (Severnaya Zemlya archipelago) prevent ice drift and lead to fast ice formation over the deep regions. The high-resolution coastline underling the form factor F_2 takes the offshore island chain into account, which leads to higher lateral drag on sea ice.

4.2 Estimation of free parameters

In this section, we test the effects of lateral drag coefficients on simulating landfast ice in the lateral drag parameterization with the static function and form factor F_2. Timeseries of total landfast ice extent are used to evaluate different model simulations. The root mean square difference (RMSD) and the mean difference (MD) of landfast ice

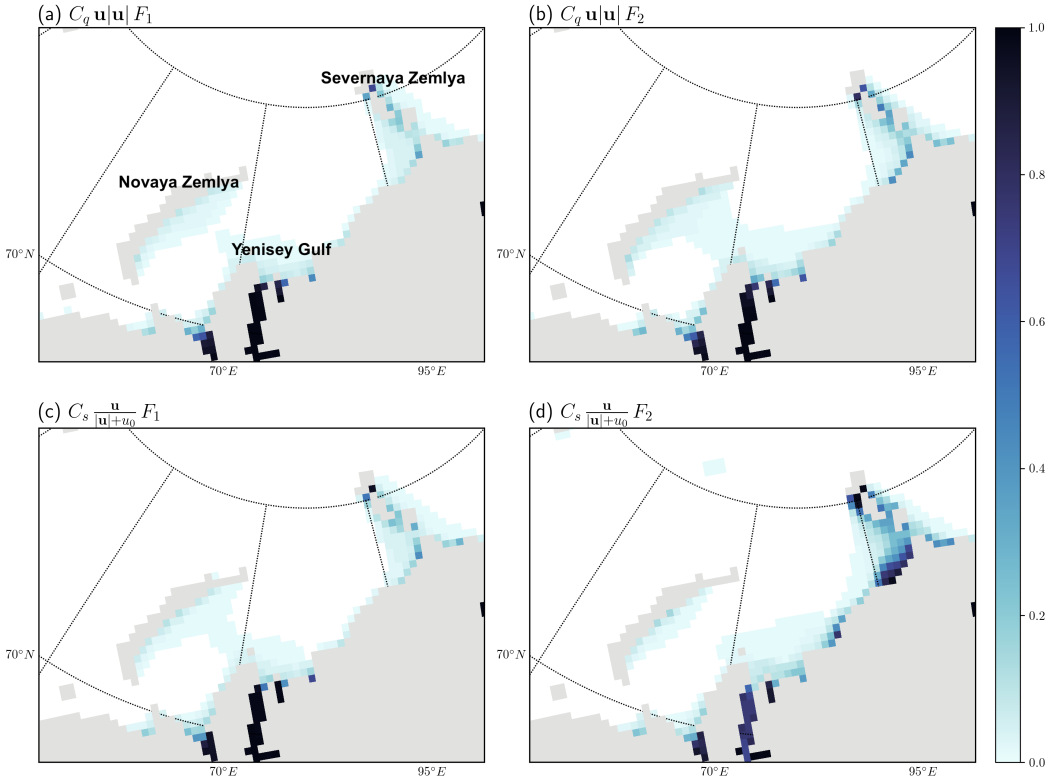

Figure 3. Landfast ice frequency from January to May in 2001–2007 in the Kara Sea with different lateral drag formulations. (a) Quadratic function with simple coast factor F_1 and $C_q = 0.1\,\mathrm{m}^{-1}$. (b) Quadratic function with normalized coastline length F_2 and $C_q = 0.1\,\mathrm{m}^{-1}$. (c) Static function with simple coast factor F_1 and $C_s = 1 \times 10^{-4}\,\mathrm{m\,s}^{-2}$. (d) Static function with normalized coastline length F_2 and $C_s = 1 \times 10^{-4}\,\mathrm{m\,s}^{-2}$. The colorbar is the landfast ice frequency, the darker the more often there is landfast ice.

extent between the model simulations and NIC data are used as metrics. We ran simulations with the lateral drag coefficients ranging from $10^{-4}\,\mathrm{m\,s^{-2}}$ to $10^{-3}\,\mathrm{m\,s^{-2}}$. We only show simulations with coefficients 1, 2, $3\times10^{-4}\,\mathrm{m\,s^{-2}}$ in Table 2 because these three simulations are closest to observations. We also studied the landfast ice extent in 2001–2007 in the Kara Sea in the LD (lateral drag only) simulations with different lateral drag coefficients (see Figure 4) compared to the CTRL simulation and NIC data. The CTRL simulation systematically underestimates landfast ice in the Kara Sea while still capturing the annual and some of the interannual variability (Figure 4). The interannual variability of landfast ice in LD simulations is generally more consistent with observations.

With different lateral drag coefficients the RMSD of landfast ice extent in the Kara Sea does not change much. The LD simulation with lateral drag coefficient $C_{s,2} = 2\times10^{-4}\,\mathrm{m\,s^{-2}}$ has the smallest RMSD ($5.44\times10^4\,\mathrm{km^2}$, Table 2). Note that the RMSD in LD simulation with $C_{s,2}$ is not small because of the landfast ice extent outliers in the year 2002 and 2006 in the Kara Sea (see Figure 4). In contrast, the mean differences distinguish LD simulations with different lateral drag coefficients. The LD simulation with a lateral drag coefficient of $C_{s,1} = 10^{-4}\,\mathrm{m\,s^{-2}}$ underestimates landfast ice in the Kara Sea ($3.27\times10^4\,\mathrm{km^2}$ less than the observation), whereas $C_{s,3} = 3\times10^{-4}\,\mathrm{m\,s^{-2}}$ leads to an overestimation of landfast ice in the Kara Sea ($1.41\times10^4\,\mathrm{km^2}$ larger than the observation). The best agreement with the NIC data, with a mean difference of $-0.60\times10^4\,\mathrm{km^2}$ in the Kara Sea, is found with $C_{s,2} = 2\times10^{-4}\,\mathrm{m\,s^{-2}}$ (Table 2).

The large RMSD and mean differences in the Laptev Sea and the East Siberian Sea show that the lateral drag parameterization underestimates landfast ice in these two regions. Because these two regions are exposed to open ocean with no arching from island chains, lateral drag cannot support landfast ice. Instead, the grounding scheme is the primary mechanism to stabilize landfast ice in the Laptev Sea and the East Siberian Sea (Lemieux et al., 2015). However, in the focus of our study, the Kara Sea, the lateral drag parameterization plays a more important role. Consequently, we use lateral drag coefficient $C_s = 2\times10^{-4}\,\mathrm{m\,s^{-2}}$ for the further analysis of this paper.

4.3 Comparison between lateral drag and basal drag parameterization

To explore different effects of lateral drag parameterization and grounding scheme, we studied the spatial distribution of landfast ice in the Arctic for different combinations

Table 2. Landfast ice extent statistics of model simulations with different lateral drag coefficients with respect to observations in 2001–2007. RMSD is root mean square deviation and MD is mean difference (in $10^4\,\mathrm{km}^2$).

Regions	$C_{s,1} = 1 \times 10^{-4}\,\mathrm{m\,s^{-2}}$		$C_{s,2} = 2 \times 10^{-4}\,\mathrm{m\,s^{-2}}$		$C_{s,3} = 3 \times 10^{-4}\,\mathrm{m\,s^{-2}}$	
	RMSD	MD	RMSD	MD	RMSD	MD
Kara Sea	5.64	-3.27	5.44	-0.60	6.64	1.41
Laptev Sea	8.95	-6.51	7.68	-5.12	6.92	-4.15
East Siberian Sea	10.90	-7.42	10.10	-6.71	9.55	-6.16
Beaufort Sea	1.68	-0.61	1.84	-0.14	1.96	0.13

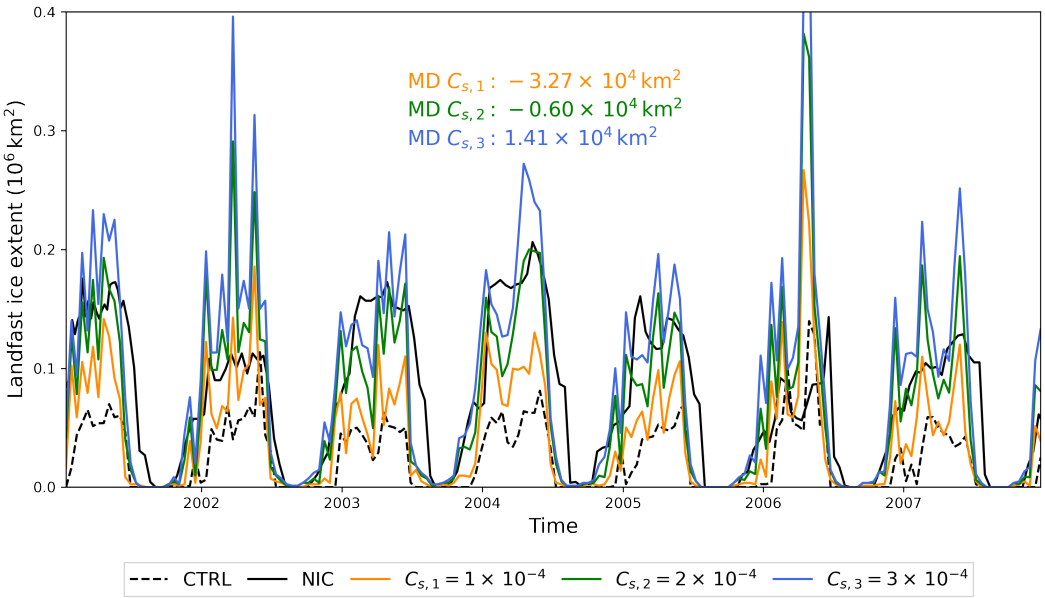

Figure 4. Landfast ice extent in Kara Sea in 2001–2007. Orange, green, and blue lines are the LD experiment with $C_{s,1} = 1 \times 10^{-4}\,\mathrm{m\,s^{-2}}$, $C_{s,2} = 2 \times 10^{-4}\,\mathrm{m\,s^{-2}}$ and $C_{s,3} = 3 \times 10^{-4}\,\mathrm{m\,s^{-2}}$, respectively. The black line is the NIC data, and the black dashed line is the CTRL simulation. The numbers show the mean differences of landfast ice extent in four regions between LDs and observation for the years 2001–2007.

of parameterizations for lateral and bottom drag (Figure 5). The tuning parameters of the grounding scheme depend on resolution. From experiments with the grounding scheme for $k_1 = 6$, 7, 8, 10 and $k_2 = 5$, 10, 15 N m^{-3} (summarized in Table A1 in the appendix) we find that, consistent with Lemieux et al. (2015), the set $k_1 = 8$, $k_2 = 15\,\mathrm{N\,m^{-3}}$ provides best agreement to the satellite data in the Laptev Sea in our configuration (RMSD=$4.55\times10^4\,\mathrm{km^2}$ and MD = $-1.06\times10^4\,\mathrm{km^2}$), but overestimated landfast ice extent in the East Siberian Sea (RMSD=$7.32\times10^4\,\mathrm{km^2}$ and MD = $3.44\times10^4\,\mathrm{km^2}$) and the Beaufort Sea (RMSD=$1.70\times10^4\,\mathrm{km^2}$ and MD = $0.18\times10^4\,\mathrm{km^2}$). Still we use this parameter combination to compare to previous results. Note that the basal drag parameterization underestimates the landfast ice extent in the Kara Sea (RMSD=$4.95\times10^4\,\mathrm{km^2}$ and MD = $-2.91\times10^4\,\mathrm{km^2}$), which is also consistent with Lemieux et al. (2015).

We use the Kara Sea as the reference region to study the lateral drag parameterization and the Laptev Sea as the reference region for the basal drag parameterization. The Kara Sea is different from the Laptev Sea in topography and water depth, so that the parameterized mechanisms that lead to landfast ice are different and most likely complementary. Therefore, we refrain from retuning all three parameters k_1, k_2, and C_s in the combination run LD+BD, but use the parameter values found in the runs LD and BD.

In the Kara Sea, the mean landfast ice extent in the LD + BD simulation is larger than in the observation by $0.88\times10^4\,\mathrm{km^2}$ (Table 3). The LD simulation reduces the mean difference of landfast ice frequency in the Kara Sea compared to observations to $-0.60\times10^4\,\mathrm{km^2}$ (Table 3) and the distribution of relative frequency in the Kara Sea also improves compared to the BD simulation (Figure 5, Figure 9). The Severnaya Zemlya archipelago in the Kara Sea provides anchor points and exerts lateral friction such that more sea ice attaches to the coast. Since the LD simulation contains additional coastline information, there is also some landfast ice in the LD simulation near Franz-Josef-Land archipelago ($\approx$ 81°N, 55°E), an archipelago that is unresolved by the model grid. The larger RMSD ($5.44\times10^4\,\mathrm{km^2}$) can be explained by the short outliers in 2002 and 2006 (see Figure 6b) when the LD simulation overestimates landfast ice in the Western Kara Sea near Novaya Zemlya. Note that the two peaks in the LD simulation two weeks before March 24, 2002 and April 16, 2006 also appear in the model simulations with grounding scheme (see Figure 6b and Lemieux et al. (2015), their Figure 6b). The BD simulation underestimates the landfast ice extent in the Kara Sea (mean difference:$-2.91\times10^4\,\mathrm{km^2}$), but improves

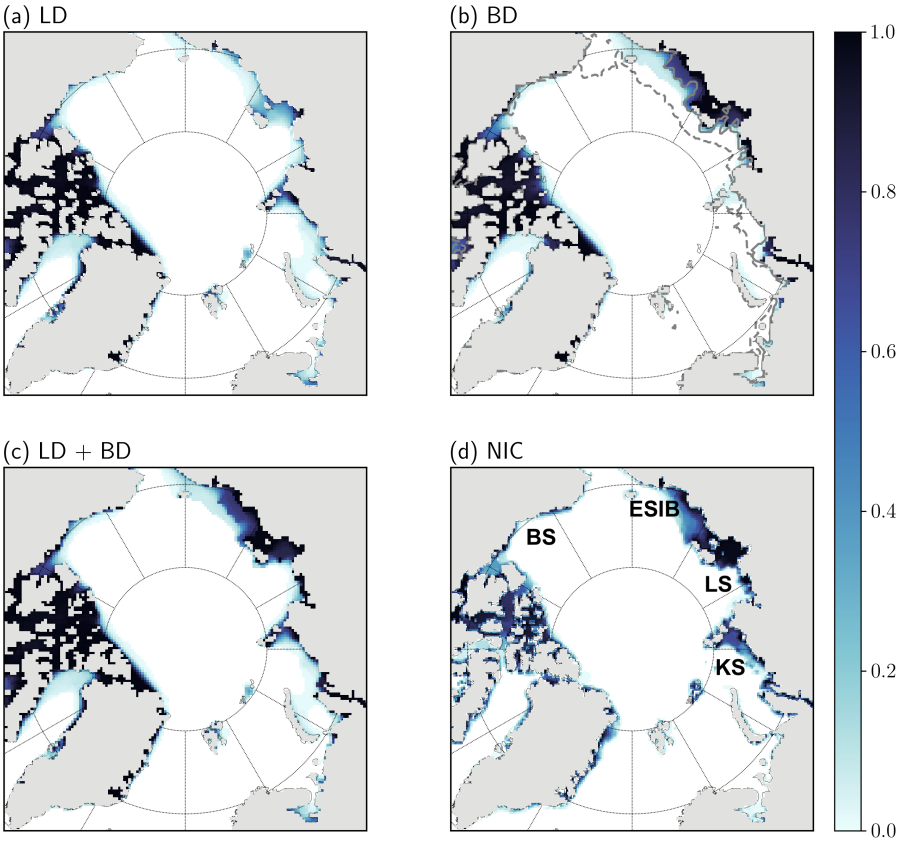

Figure 5. Landfast ice frequency for January to May in 2001–2007 in the Arctic. (a) LD with lateral drag $C_s = 2 \times 10^{-4}\,\mathrm{m\,s^{-2}}$. (b) BD with basal drag $k_1 = 8$, $k_2 = 15\,\mathrm{N\,m^{-3}}$. The solid and dashed isolines represent the 25 m and the 60 m depth contours. (c) LD + BD with lateral drag coefficient $C_s = 2 \times 10^{-4}\,\mathrm{m\,s^{-2}}$, $k_1 = 8$, $k_2 = 15\,\mathrm{N\,m^{-3}}$. (d) NIC data. BS: Beaufort Sea, ESIB: East Siberian Sea, LS: Laptev Sea, KS: Kara Sea.

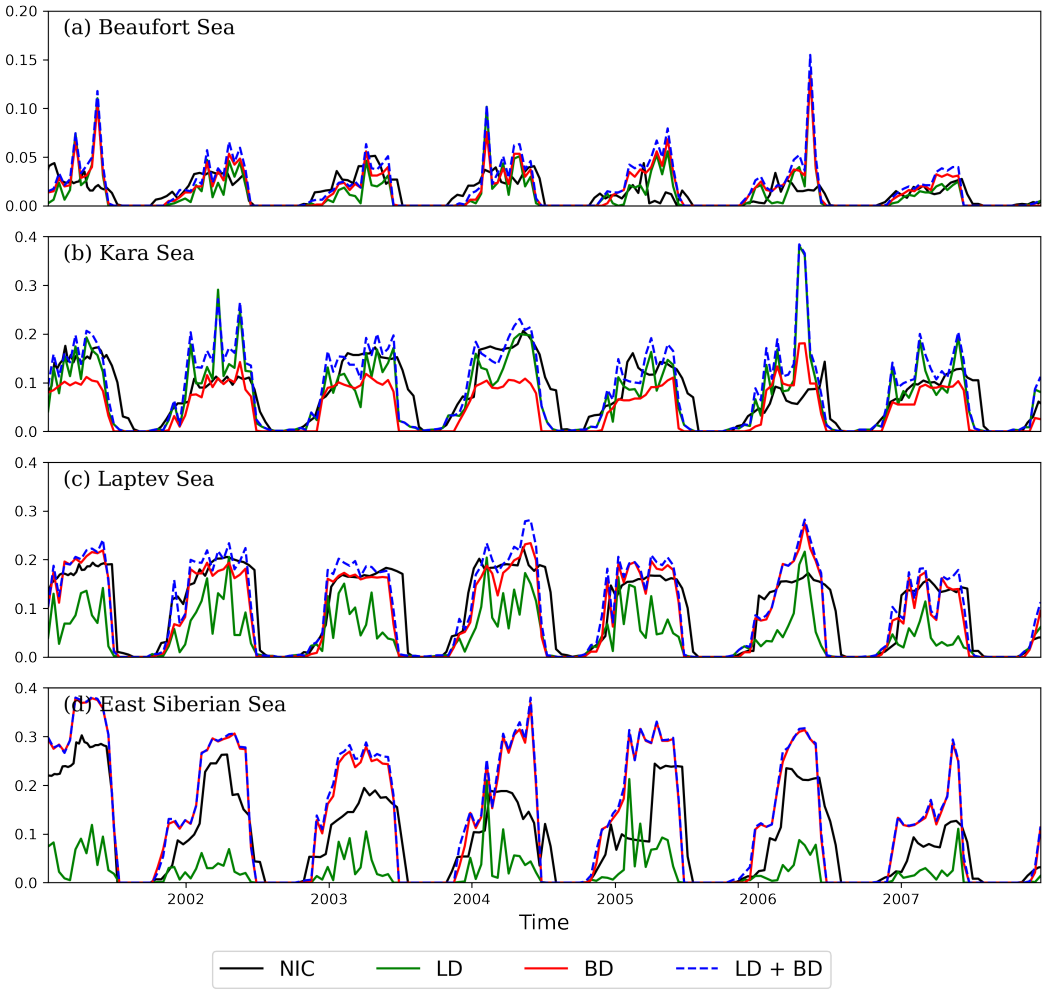

Figure 6. Time series of landfast ice extent (10^6 km^2) in four regions: (a) the Beaufort Sea; (b) the Kara Sea; (c) the Laptev Sea; and (d) the East Siberian Sea.

it near the Yenisey Gulf compared to the LD simulation (Figure 5b), because the scheme successfully parameterizes the grounding pressure ridges in this shallow region (McClelland et al., 2012; Harms, 2004).

The mean landfast ice extent in the Laptev Sea in the LD + BD simulation is on average 0.05×10^4 km^2 smaller than the observation (Table 3). Combining the lateral and basal drag parameterizations reduces the mean differences compared to lateral drag or basal drag parameterization alone in the Laptev Sea. However, larger differences were found in the East Siberian and the Beaufort Sea. Note that the mean differences of landfast ice extent in LD + BD simulation in the East Siberian Sea and the Beaufort Sea (3.82×10^4 km^2 and 0.49×10^4 km^2) are slightly larger than that in the simulation only using

Table 3. Landfast ice statistics of different model simulations with respect to observations in 2001–2007 (in $10^4\,km^2$).

Regions	LD		BD		LD + BD	
	RMSD	MD	RMSD	MD	RMSD	MD
Kara Sea	5.44	-0.60	4.95	-2.91	5.61	0.88
Laptev Sea	7.68	-5.12	4.55	-1.06	4.64	-0.05
East Siberian Sea	10.10	-6.71	7.32	3.44	7.63	3.82
Beaufort Sea	1.84	-0.14	1.70	0.18	2.05	0.49

BD simulation. On average, the combination of lateral and basal drag improves the landfast ice simulations in all Arctic marginal seas.

4.4 Comparison of large scale features between CTRL and LD simulation

The SIC and sea ice thickness (SIT) in the model simulations with lateral drag parameterization in April 2001–2007 are examined in this section. Compared to the sea ice concentration and thickness from the CTRL simulation, SIC differs in the marginal ice zone (MIZ), while SIT differs near offshore shelves (not shown). As expected, the lateral drag parameterization does not directly influence regions far away from the coast.

From time series of sea ice volume and sea ice extent over the Arctic domain in 2001–2007 (Figure 7), the RMSD for the sea ice volume between LD simulation and the Panarctic Ice Ocean Modeling and Assimilation System (PIOMAS, Zhang & Rothrock, 2003; Schweiger et al., 2011) is $5.44\times10^3\,km^3$. The RMSD for the sea ice volume between the LD and CTRL simulations is $0.47\times10^3\,km^3$. The LD (LD+BD) simulation leads to a very similar sea ice volume and extent compared to the CTRL simulation. The RMSD of sea ice extent between LD simulations and estimates of the Arctic Data archive System (ADS) Quasi-real-time polar environment observation monitor (Yabuki et al., 2011) is $1.35\times10^6\,km^2$. The RMSD of sea ice extent between the LD simulation and the CTRL simulation is $0.06\times10^6\,km^2$. Generally, the lateral drag parameterization slightly decreases the mean ice thickness (i.e., volume) by 1.9% compared to the CTRL simulation, but otherwise has little effect on the large scale properties of the solution.

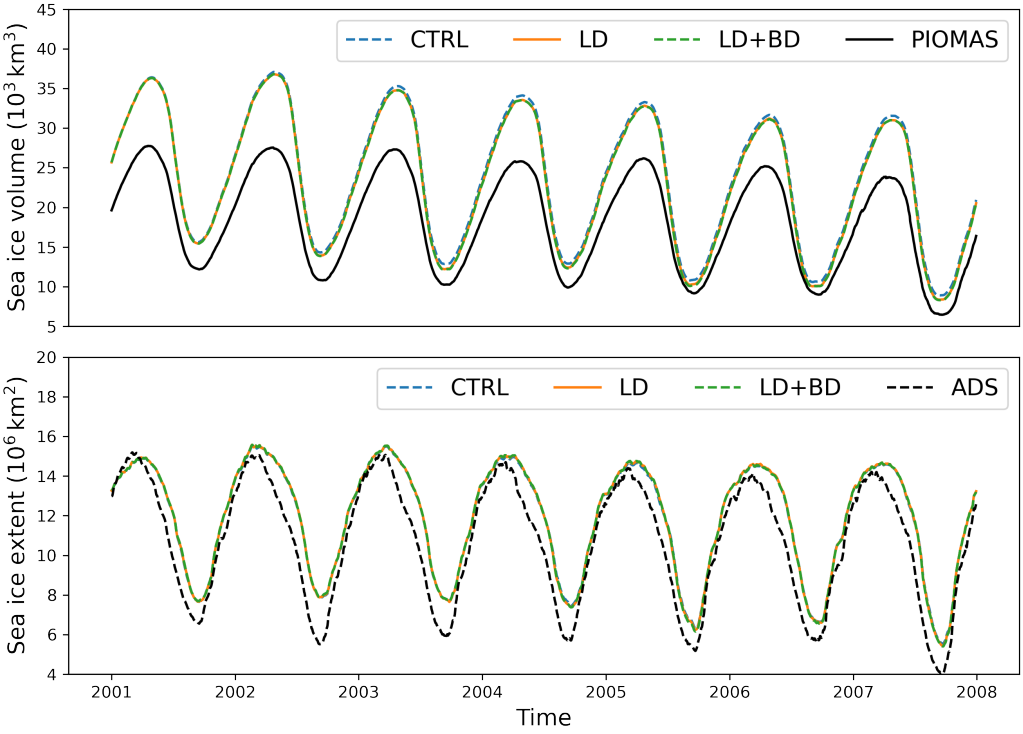

Figure 7. Time series of sea ice volume and sea ice extent over the arctic in 2001–2007. The reference data for sea ice volume and sea ice extent is from PIOMAS and ADS, respectively.

5 Discussion

The results presented in Section 4 demonstrate that the mechanism for landfast ice formation largely depends on geography. Grounding is the dominant mechanism to form landfast ice in regions shallower than a critical depth. In contrast, lateral drag stress is more important in regions exceeding the critical water depth, where island chains provide pinning points for sea ice arches. However, the lateral drag parameterization cannot replace, but can only augment the grounding scheme because by itself it produces too little landfast ice in the shallow regions (i.e., the Laptev Sea and the East Siberian Sea where there are no islands to act as anchor points). Both physical processes should be parameterized to simulate landfast ice in the entire Arctic.

The lateral drag parameterization improves the landfast ice simulation in the Kara Sea, but it overestimates landfast ice in the Western Kara Sea in March 2002 and April 2006. We investigated one-week averaged wind velocity and sea ice thickness before March 24, 2002 and April 16, 2006 to explore potential reasons for the overestimation of landfast ice. Two time periods for the same date in 2005 and 2007 were also picked for comparison. Here we provide two hypotheses to explain this phenomenon. One of the hypotheses is related to the wind direction leading to the anomalous landfast ice. When the wind blows perpendicular to Novaya Zemlya, there is excessive landfast ice in the Western Kara Sea. Sea ice piles up in the Western Kara Sea, attaches to the coast, and becomes land fast (see Figure 8a, 8b). However, when the wind blows parallel to the coast, there is no landfast ice in the Western Kara Sea (Figure 8d). The second hypothesis is a combination of local wind patterns and landfast ice diagnostics artifacts. During the observed periods of high landfast ice in the Western Kara Sea in 2002 and 2006, there were anticyclonic wind patterns around the Kara Sea, which may have led to Ekman convergence, where the ice is not moved away but "pushed together" in convergence (Figure 8b). As a consequence, the immobile sea ice is falsely diagnosed as landfast ice. These processes may also lead to the higher temporal variability in land fast ice compared to observations (see Figure 6). A similar process reduces sea ice speed, albeit at larger scales in the Beaufort Sea, when ice concentration and internal stresses are high in wintertime during an anticyclonic anomaly (Wang et al., 2019).

As a test, we calculate the landfast ice frequency in the Kara Sea from January to May in 2001–2007, excluding March 2002 and April 2006. The results show a close agree-

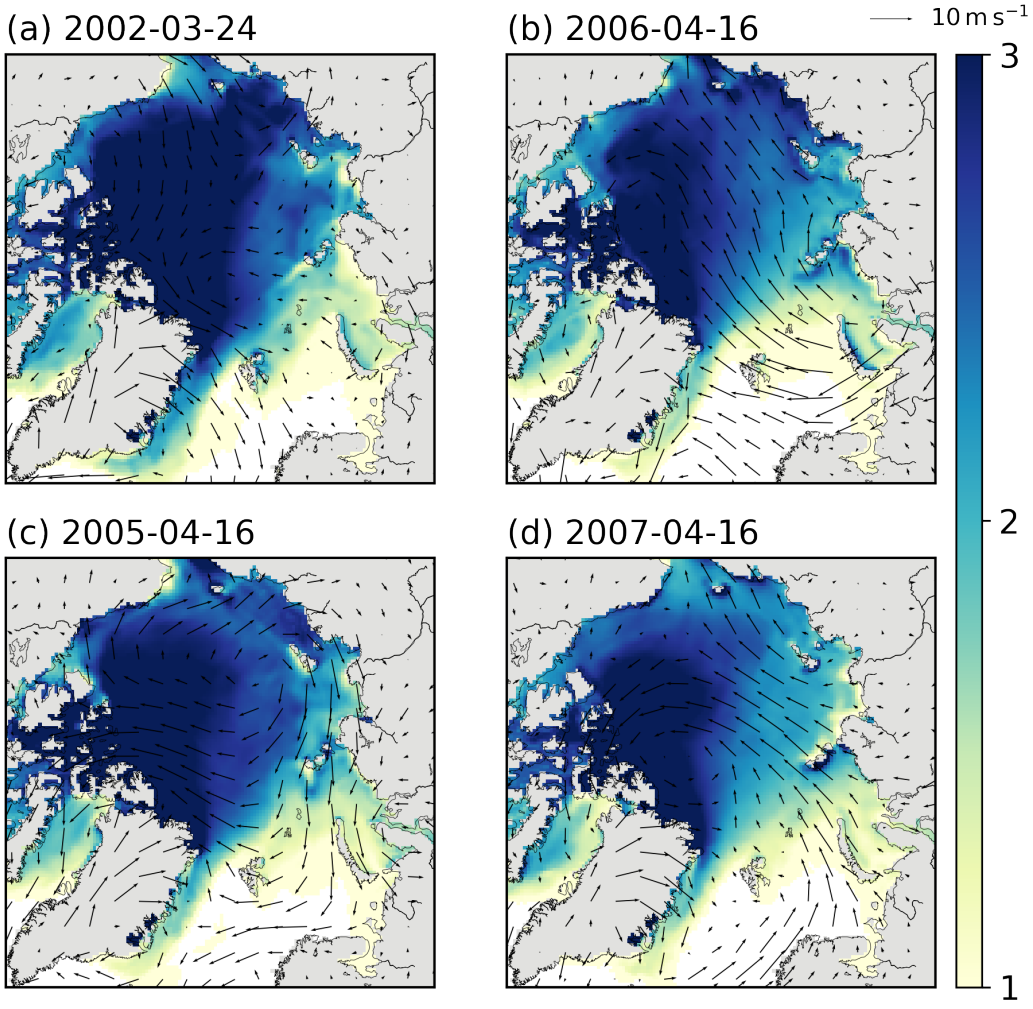

Figure 8. One week average of sea ice thickness (m) and wind velocity ($m\,s^{-1}$) before: (a) 24 March 2002 (high landfast ice); (b) 16 April 2006 (high landfast ice); (c) 16 April 2005 (for reference); (d) 16 April 2007 (for reference). The colorbar describes the sea ice thickness (m), the wind velocity reference is $10\,m\,s^{-1}$.

399 ment with the NIC data for the simulations with lateral drag parameterization alone and
400 the combination of lateral drag parameterization and grounding scheme in the Kara Sea
401 (Figure 9).

402 Attempts to improve landfast ice simulation in the Kara Sea by modifying global
403 parameters in the sea ice model, for example, implementing a large maximum viscosity
404 in a regional sea ice model (Olason, 2016), or adding tensile strength to the rheology (Beatty
405 & Holland, 2010; Lemieux et al., 2016) were successful. However, they have the disad-

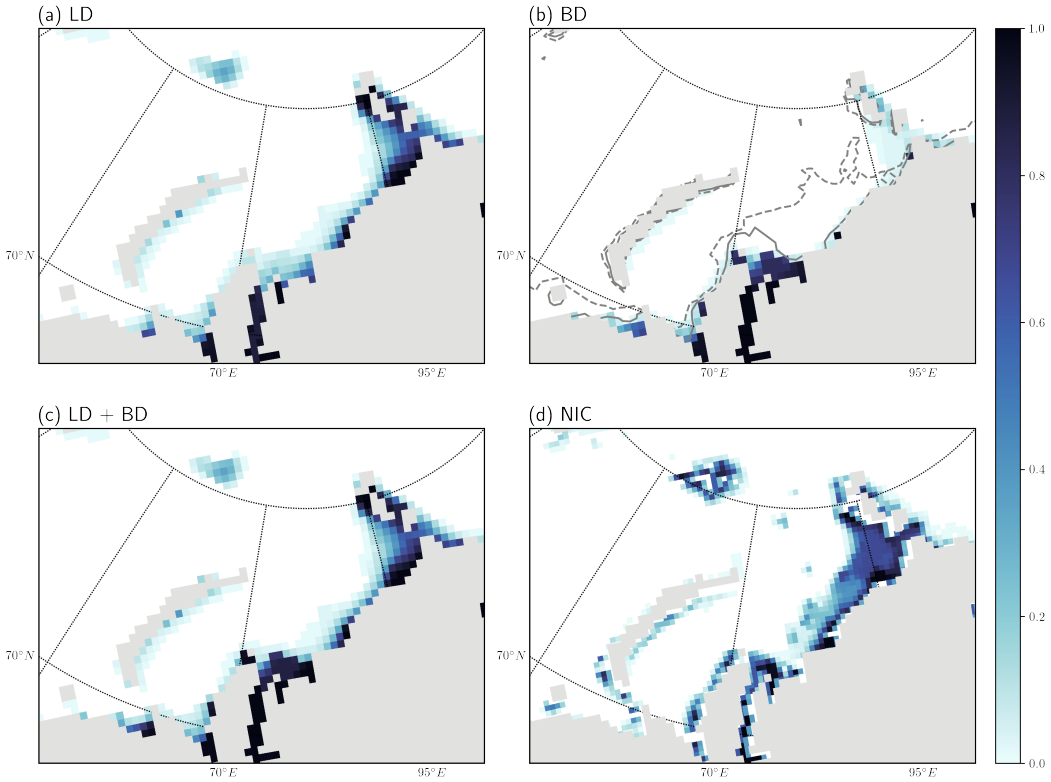

Figure 9. Landfast ice frequency for January to May in 2001–2007 in the Kara Sea with data in the two weeks with exceptionally large landfast ice in 2002 and 2006 excluded. The solid and dashed isolines in (b) represent the 25 m and the 60 m depth contours in the Kara Sea.

vantage that they affect the sea ice dynamics in the entire Arctic. In contrast, the approaches based on domain geometry such as the depth-dependent grounding scheme or our new lateral drag scheme along coastlines affect the pan-Arctic scale far away from the coasts only indirectly. The form factor in the lateral drag parameterization allows including additional subgrid information independent of model resolution. This extra information leads to realistic effects of unresolved coastline in the coarse model.

Implementation of the lateral drag parameterization is very simple and improves landfast ice estimates in the deep regions in the Arctic. Landfast ice in Antarctica is often attached to grounded icebergs which ground in water depth of 400-500 m or to other coastal features (e.g., the shoreline, glacier tongues, and ice shelves, Massom et al., 2001; Fraser et al., 2012, 2020). Because of the deep topography in Antarctica, the grounding scheme may not work as well as in the Arctic. Including our lateral drag parameterization in an Antarctic sea ice model may lead to realistic landfast ice simulations.

6 Conclusion

This paper introduces a lateral drag parameterization to improve landfast ice simulation in the Arctic region. The lateral drag parameterization replaces the common no-slip boundary condition in the sea ice momentum equation by a lateral stress term, which is a function of sea ice velocity, and coastline features. We assume that lateral friction is a static function of sea ice velocity and generate a form factor to represent the complexity of the coastline. Numerical experiments were conducted with an Arctic sea ice-ocean model with a grid spacing of 36 km. The landfast ice extent and frequency of model simulations with lateral drag parameterization and grounding schemes were examined in four regions: the Kara Sea, the Laptev Sea, the East Siberian Sea, and the Beaufort Sea. Compared to no parameterization and grounding scheme, lateral drag parametrization leads to a more realistic landfast ice area in the Kara Sea.

Although lateral drag parameterization successfully simulates landfast in the Kara Sea, it underestimates landfast ice in the East Siberian Sea, Laptev, and the Beaufort Sea compared to the grounding scheme, because the mechanism of landfast ice formation is different in these regions. The combination of lateral and basal drag parameterization leads to the most realistic estimates of landfast ice in space and time and captures most of the annual cycle and the interannual variability in the Arctic. Thus, we

recommend using the lateral and basal drag parameterization in combination to simulate landfast ice in the Arctic Ocean accurately.

Appendix A Appendix for the statistics in the BD simulations

Acknowledgments

The authors thank Bruno Tremblay for the suggestions of the static friction form of the form factor in the paper and Damien Ringeisen for writing suggestions. This work is supported under DFG-funded International Research Training Group ArcTrain (IRTG 1904 ArcTrain).

Code availability. The code of the lateral drag parameterization in MITgcm is available at `https://github.com/yqliu11/MITgcm/tree/seaice_lateraldrag_v3`.

References

Adcroft, A., & Marshall, D. (1998). How slippery are piecewise-constant coastlines in numerical ocean models? *Tellus A: Dynamic Meteorology and Oceanography*, *50*(1), 95–108. doi: 10.3402/tellusa.v50i1.14514

Beatty, C. K., & Holland, D. M. (2010). Modeling landfast sea ice by adding tensile strength. *Journal of Physical Oceanography*, *40*(1), 185–198. doi: 10.1175/2009JPO4105.1

Berrisford, P., Dee, D., Poli, P., Brugge, R., Fielding, K., Fuentes, M., ... Simmons, A. (2011). *The ERA-Interim Archive* (Tech. Rep.). ECMWF. Retrieved from `https://www.ecmwf.int/node/8174`

Divine, D. V., Korsnes, R., Makshtas, A. P., Godtliebsen, F., & Svendsen, H. (2005). Atmospheric-driven state transfer of shore-fast ice in the northeastern Kara Sea. *Journal of Geophysical Research: Oceans*, *110*(9), 1–13. doi: 10.1029/2004JC002706

Fraser, A. D., Massom, R. A., Michael, K. J., Galton-Fenzi, B. K., & Lieser, J. L. (2012). East Antarctic landfast sea ice distribution and variability, 2000-08. *Journal of Climate*, *25*(4), 1137–1156. doi: 10.1175/JCLI-D-10-05032.1

Fraser, A. D., Massom, R. A., Ohshima, K. I., Willmes, S., Kappes, P. J., Cartwright, J., & Porter-Smith, R. (2020). High-resolution mapping of circum-Antarctic landfast sea ice distribution, 2000-2018. *Earth System Science Data*,

Table A1. RMSD of model simulations with basal drag parameterization with respect to observations in 2001–2007 in four marginal seas ($10^4\,km^2$).

	RMSD				MD			
	Kara Sea	Laptev Sea	East Siberian Sea	Beaufort Sea	Kara Sea	Laptev Sea	East Siberian Sea	Beaufort Sea
$k_1 = 6, k_2 = 5$	6.16	6.21	5.20	1.64	-4.35	-3.76	-1.56	-0.24
$k_1 = 6, k_2 = 10$	5.97	5.96	5.25	1.65	-4.15	-3.44	-1.24	-0.19
$k_1 = 6, k_2 = 15$	5.88	5.88	5.29	1.65	-4.04	-3.33	-1.09	-0.17
$k_1 = 7, k_2 = 5$	5.57	5.52	5.37	1.66	-3.75	-2.93	0.58	-0.09
$k_1 = 7, k_2 = 10$	5.34	5.29	5.65	1.64	-3.55	-2.6	1.23	-0.02
$k_1 = 7, k_2 = 15$	5.23	5.17	5.79	1.66	-3.4	-2.44	1.54	0.02
$k_1 = 8, k_2 = 5$	5.13	4.79	6.43	1.68	-3.27	-1.9	2.50	0.08
$k_1 = 8, k_2 = 10$	5.02	4.63	7.06	1.68	-3.03	-1.46	3.15	0.14
$k_1 = 8, k_2 = 15$	4.95	4.55	7.32	1.70	-2.91	-1.06	3.44	0.18
$k_1 = 10, k_2 = 5$	4.86	5.27	9.75	1.76	-2.51	0.82	5.53	0.34
$k_1 = 10, k_2 = 10$	4.71	5.63	10.60	1.77	-2.17	1.40	6.40	0.39
$k_1 = 10, k_2 = 15$	9.55	12.30	12.60	1.84	-7.48	-9.51	-8.89	-1.28

12(4), 2987–2999. doi: 10.5194/essd-12-2987-2020

Harms, I. (2004). *Polar seas oceanography: An integrated case study of the Kara Sea* (Vol. 85) (No. 8). London, U. K.: Springer. doi: 10.1029/2004eo080011

Hibler, W. D. (1979). A dynamic thermodynamic sea ice model. *Journal of Physical Oceanography*, *9*(4), 815–846. doi: 10.1175/1520-0485(1979)009⟨0815:adtsim⟩2.0.co;2

Howell, S. E., Laliberté, F., Kwok, R., Derksen, C., & King, J. (2016). Landfast ice thickness in the Canadian Arctic Archipelago from observations and models. *Cryosphere*, *10*(4), 1463–1475. doi: 10.5194/tc-10-1463-2016

Itkin, P., Losch, M., & Gerdes, R. (2015). Landfast ice affects the stability of the Arctic halocline: Evidence from a numerical model. *Journal of Geophysical Research: Oceans*, *120*(4), 2622–2635. doi: 10.1002/2014JC010353

Jakobsson, M., Mayer, L., Coakley, B., Dowdeswell, J. A., Forbes, S., Fridman, B., ... Weatherall, P. (2012). The international bathymetric chart of the Arctic Ocean (IBCAO) Version 3.0. *Geophysical Research Letters*, *39*(12), 1–6. doi: 10.1029/2012GL052219

Johnson, M., Proshutinsky, A., Aksenov, Y., Nguyen, A. T., Lindsay, R., Haas, C., ... De Cuevas, B. (2012). Evaluation of Arctic sea ice thickness simulated by Arctic Ocean model intercomparison project models. *Journal of Geophysical Research: Oceans*, *117*(3). doi: 10.1029/2011JC007257

Kwok, R. (2018). Arctic sea ice thickness, volume, and multiyear ice coverage: Losses and coupled variability (1958-2018). *Environmental Research Letters*, *13*(10), 105005. doi: 10.1088/1748-9326/aae3ec

Lemieux, J. F., Dupont, F., Blain, P., Roy, F., Smith, G. C., & Flato, G. M. (2016). Improving the simulation of landfast ice by combining tensile strength and a parameterization for grounded ridges. *Journal of Geophysical Research: Oceans*, *121*(10), 7354–7368. doi: 10.1002/2016JC012006

Lemieux, J. F., Lei, J., Dupont, F., Roy, F., Losch, M., Lique, C., & Laliberté, F. (2018). The impact of tides on simulated landfast ice in a pan-Arctic ice-ocean model. *Journal of Geophysical Research: Oceans*, *123*(11), 7747–7762. doi: 10.1029/2018JC014080

Lemieux, J. F., Tremblay, L. B., Dupont, F., Plante, M., Smith, G. C., & Dumont, D. (2015). A basal stress parameterization for modeling landfast

ice. *Journal of Geophysical Research: Oceans*, *120*(4), 3157–3173. doi: 10.1002/2014JC010678

Li, Z., Zhao, J., Su, J., Li, C., Cheng, B., Hui, F., ... Shi, L. (2020). Spatial and temporal variations in the extent and thickness of Arctic landfast ice. *Remote Sensing*, *12*(1), 64. doi: 10.3390/RS12010064

Losch, M., Menemenlis, D., Campin, J. M., Heimbach, P., & Hill, C. (2010). On the formulation of sea-ice models. Part 1: Effects of different solver implementations and parameterizations. *Ocean Modelling*, *33*(1-2), 129–144. doi: 10.1016/j.ocemod.2009.12.008

Mahoney, A., Eicken, H., Gaylord, A. G., & Shapiro, L. (2007). Alaska landfast sea ice: Links with bathymetry and atmospheric circulation. *Journal of Geophysical Research: Oceans*, *112*(2). doi: 10.1029/2006JC003559

Mahoney, A. R., Eicken, H., Gaylord, A. G., & Gens, R. (2014). Landfast sea ice extent in the Chukchi and Beaufort Seas: The annual cycle and decadal variability. *Cold Regions Science and Technology*, *103*, 41–56. doi: 10.1016/j.coldregions.2014.03.003

Marshall, J., Adcroft, A., Hill, C., Perelman, L., & Heisey, C. (1997). A finite-volume, incompressible Navier Stokes model for studies of the ocean on parallel computers. *Journal of Geophysical Research: Oceans*, *102*(C3), 5753–5766. doi: 10.1029/96JC02775

Massom, R. A., Hill, K. L., Lytle, V. I., Worby, A. P., Paget, M. J., & Allison, I. (2001). Effects of regional fast-ice and iceberg distributions on the behaviour of the Mertz Glacier polynya, East Antarctica. *Annals of Glaciology*, *33*, 391–398. doi: 10.3189/172756401781818518

McClelland, J. W., Holmes, R. M., Dunton, K. H., & Macdonald, R. W. (2012). The Arctic Ocean estuary. *Estuaries and Coasts*, *35*(2), 353–368. doi: 10.1007/s12237-010-9357-3

Melling, H. (2002). Sea ice of the northern Canadian Arctic Archipelago. *Journal of Geophysical Research: Oceans*, *107*(11). doi: 10.1029/2001jc001102

MITgcm Group. (2020). *MITgcm User Manual.* Cambridge, MA 02139, USA. Retrieved from `https://doi.org/10.5281/zenodo.1409237`

National Ice Center, Compiled by F. Fetterer and C. Fowler. (2009). *U.S. National Ice Center Arctic sea ice charts and climatologies in gridded Format, 1972 -*

2007, Version 1. Boulder, Colorado USA. doi: 10.7265/N5X34VDB

Olason, E. (2016). A dynamical model of Kara Sea land-fast ice. *Journal of Geophysical Research: Oceans*, *121*(5), 3141–3158. doi: 10.1002/2016JC011638

Proshutinsky, A., Ashik, I., Häkkinen, S., Hunke, E., Krishfield, R., Maltrud, M., ... Zhang, J. (2007). Sea level variability in the Arctic Ocean from AOMIP models. *Journal of Geophysical Research*, *112*(4). doi: 10.1029/2006JC003916

Rapp, B. E. (2017). *Microfluidics: Modelling, mechanics and mathematics.* William Andrew. doi: 10.1016/C2012-0-02230-2

Schweiger, A., Lindsay, R., Zhang, J., Steele, M., Stern, H., & Kwok, R. (2011). Uncertainty in modeled Arctic sea ice volume. *Journal of Geophysical Research: Oceans*, *116*(9), C00D06. doi: 10.1029/2011JC007084

Steele, M., Morley, R., & Ermold, W. (2001). PHC: A global ocean hydrography with a high-quality Arctic Ocean. *Journal of Climate*, *14*(9), 2079–2087. doi: 10.1175/1520-0442(2001)014⟨2079:PAGOHW⟩2.0.CO;2

Timmermans, M. L., & Marshall, J. (2020). Understanding Arctic Ocean circulation: A review of ocean dynamics in a changing climate. *Journal of Geophysical Research: Oceans*, *125*(4). doi: 10.1029/2018JC014378

Ungermann, M., & Losch, M. (2018). An observationally based evaluation of subgrid scale ice thickness distributions simulated in a large-scale sea ice-ocean model of the Arctic Ocean. *Journal of Geophysical Research: Oceans*, *123*(11), 8052–8067. doi: 10.1029/2018JC014022

Wang, Q., Marshall, J., Scott, J., Meneghello, G., Danilov, S., & Jung, T. (2019). On the feedback of ice-ocean stress coupling from geostrophic currents in an anticyclonic wind regime over the Beaufort Gyre. *Journal of Physical Oceanography*, *49*(2), 369–383. doi: 10.1175/JPO-D-18-0185.1

World Meteorological Organization. (2014). *WMO Sea ice nomenclature. Volume 1 Terminology.* Geneva: World Meteorological Organization. Retrieved from `https://library.wmo.int/doc_num.php?explnum_id=4651`

Yabuki, H., Park, H., Kawamoto, H., Suzuki, R., Razuvaev, V., Bulygina, O., & Ohata, T. (2011). *Baseline meteorological data in siberia (BMDS) version 5.0, Arctic data archive system (ADS).* Retrieved from `https://ads.nipr.ac.jp/dataset/A20131107-002`

Yu, Y., Stern, H., Fowler, C., Fetterer, F., & Maslanik, J. (2014). Interannual

variability of Arctic landfast ice between 1976 and 2007. *Journal of Climate*, *27*(1), 227–243. doi: 10.1175/JCLI-D-13-00178.1

Zhai, M., Cheng, B., Leppäranta, M., Hui, F., Li, X., Demchev, D., ... Cheng, X. (2021). The seasonal cycle and break-up of landfast sea ice along the northwest coast of Kotelny Island, East Siberian Sea. *Journal of Glaciology*, 1–13. doi: 10.1017/jog.2021.85

Zhang, J., & Hibler, W. D. (1997). On an efficient numerical method for modeling sea ice dynamics. *Journal of Geophysical Research: Oceans*, *102*(C4), 8691–8702. doi: 10.1029/96JC03744

Zhang, J., & Rothrock, D. A. (2003). Modeling global sea ice with a thickness and enthalpy distribution model in generalized curvilinear coordinates. *Monthly Weather Review*, *131*(5), 845–861. doi: 10.1175/1520-0493(2003)131⟨0845:MGSIWA⟩2.0.CO;2